JOURNAL OF GEOPHYSICAL RESEARCH, VOL. 89, NO. C2, PAGES 2041–2051, MARCH 20, 1984

Seasonal Variation in Wind Speed and Sea State From Global Satellite Measurements

DAVID T. SANDWELL AND RUSSELL W. AGREEN

National Geodetic Survey, National Oceanic and Atmospheric Administration

The GEOS 3 altimeter, which collected data intermittently for nearly 4 years, has measured significant wave heights and surface wind speeds over most of the world's oceans. Using these data, we have constructed contour maps of spatial variations in sea state and wind speed for winter and summer. To obtain reliable averages in the southern oceans, we low-pass filtered the data using a two-dimensional Gaussian filter with a half width of 600 km. The wind speed maps show that the zonal surface wind patterns, such as the westerlies, the horse latitudes, the trade winds, and the doldrums, shift south by about 10° between winter and summer. As expected, the highest wind speeds and sea states occur during the winter months in the mid-latitudes, 30°–60°. The most striking feature of the maps, however, is the large asymmetry in the summer to winter variation between the two hemispheres. The largest seasonal variations in sea state and wind speed occur in the northern hemisphere oceans and especially in the North Atlantic, where there is almost a factor of 2 variation. In contrast, the summer to winter variation in wind speed and sea state in the southern hemisphere oceans is relatively small. For example, the summer to winter increase in wind speed at 50°S is less than 10%, while at 50°N it is more than 50%. This differing variability can be attributed to the asymmetric distribution of continental area between the two hemispheres and the low effective heat capacity of the continents relative to the oceans.

INTRODUCTION

Remote sensing of the sea surface by orbiting radar altimeters such as GEOS 3 and Seasat has proven to be an accurate and efficient method for measuring sea surface undulations over a variety of horizontal length scales. The longer-wavelength sea surface undulations have been derived from a combination of the travel time measurements of the reflected radar pulse and orbital tracking information. An overview of the GEOS 3 mission appears in the work of *Stanley* [1979]. Departures of 100 m or more in the shape of the ocean surface from an oblate ellipsoid are caused mainly by variations in the earth's gravity field. Superimposed upon these geoid undulations are 1- to 2-m sea surface undulations associated with ocean currents and eddies.

In addition to measuring the shape of the earth, information about the sea surface conditions can be extracted from radar altimeter data. As the radar pulse reflects off an area of the sea surface several kilometers in diameter, its shape changes because of the differences in distance between the satellite and the crests/troughs of surface waves which have characteristic wavelengths of 50 to 300 m. Also, during the reflection a portion of the energy is scattered by ripples on the sea surface with wavelengths greater than several centimeters. Thus three distinct properties of the reflected radar pulse (travel time, pulse shape, and pulse amplitude) provide information about sea surface topography, sea surface waves, and sea surface roughness, respectively. The theoretical and observational relationships between return pulse shape and significant wave height $H_{1/3}$ (i.e., the height of the highest one third of the surface waves) have been discussed previously [*Fedor et al.*, 1979; *Walsh*, 1979; *Parsons*, 1979; *Mognard and Lago*, 1979]. Extracting wind speed information from the energy of the reflected pulse is less straightforward, since the backscattered power is inversely related to the mean square slope of the sea surface [*Brown*, 1979] and is not a direct measure of wind speed. However, *Cox and Munk* [1954] developed an empirical relationship between mean square sea surface slope and surface wind speed. Using this approach, *Brown* [1979] and *Mognard and Lago* [1979] developed algorithms for computing wind speed from backscatter power. After calibration their results compare favorably with ship and buoy wind speed measurements.

This study summarizes the sea state and wind speed results derived from the GEOS 3 altimeter data. A knowledge of both the spatial and the temporal variations in these quantities is important not only for weather prediction [*McPherson et al.*, 1979], but also for studies of air-sea interactions [*Charnock*, 1955; *Wu*, 1980] and investigations of wind-driven ocean circulation [*Sverdrup*, 1947].

Spatial variations in sea state and wind speed have been mapped from data acquired by the Seasat altimeter. These maps reveal a number of new and interesting features of the global sea state and wind speed patterns during the period June 28, 1978, to October 10, 1978 [*Chelton et al.*, 1981]. Moreover, a detailed study of these data over the southern ocean shows that regions of high winds and waves migrate in longitude around Antarctica [*Mognard et al.*, 1983]. These results from the Seasat mission indicate that future altimetric satellites will provide more detailed information about sea surface conditions.

While Seasat was highly successful in mapping the global distribution of sea state and wind speed, it was unable to recover much information about their temporal variations, because of its short life span. Undoubtedly, the largest time variations have a period of 1 year. To obtain a reliable estimate of the seasonal variation, these quantities must be measured for a number of years.

The GEOS 3 altimeter, which was launched in April 1975, operated for nearly 4 years (April 1975 to December 1978) and collected wave height and wind speed information intermittently during this time. A limitation of the GEOS 3 altimeter was that it could not store its data between times of ground communication. Therefore the geographical distribution of GEOS 3 data is very nonuniform when compared with the

Paper number 3C1719.

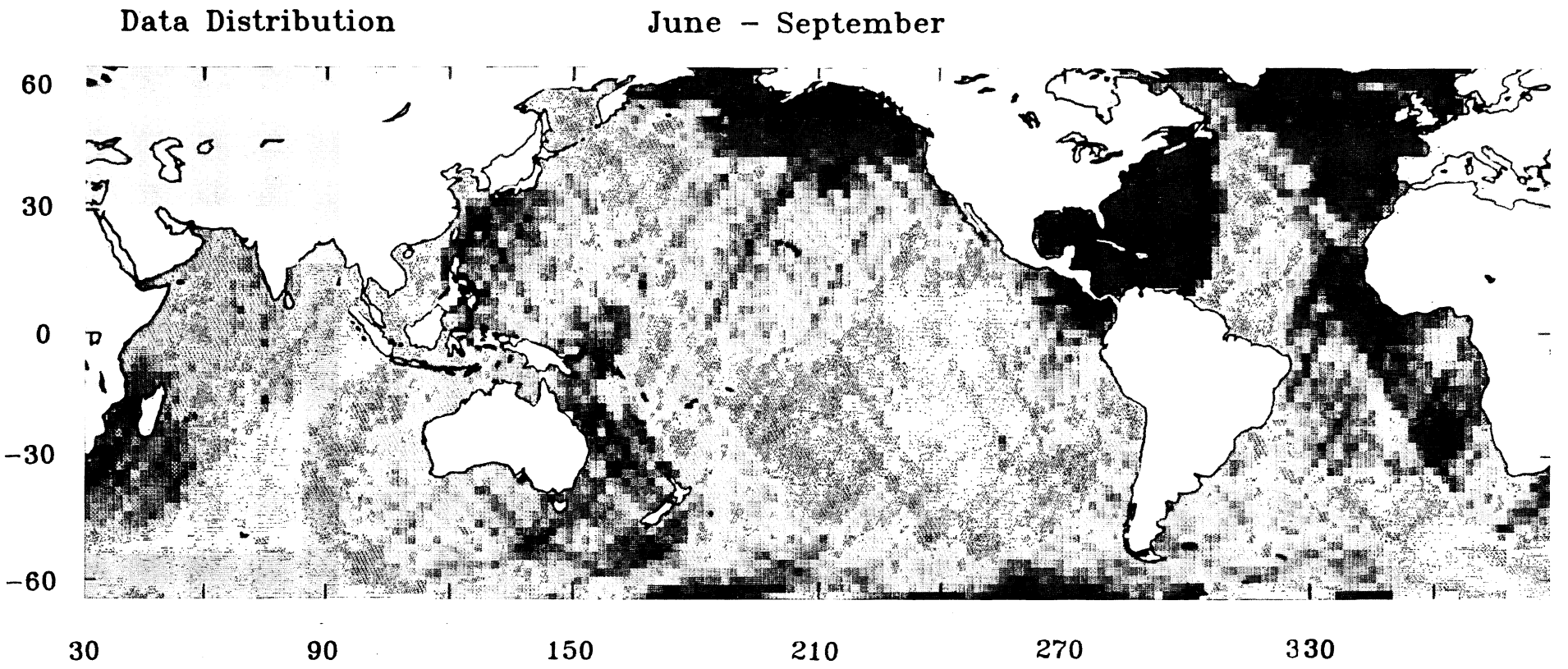
Data Distribution
June - September
60
30
0
-30
-60
30
90
150
210
270
330

Fig. 1*a*

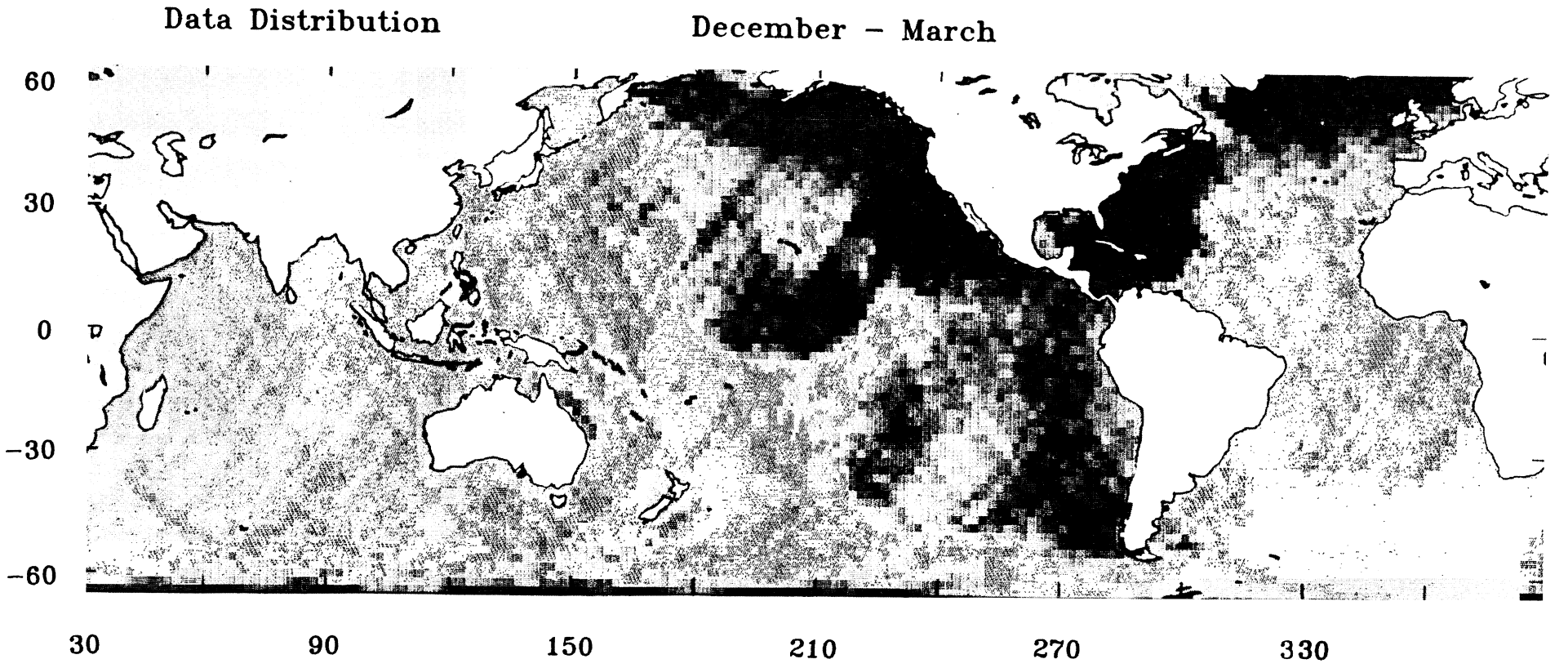

Fig. 1*b*

Fig. 1. Data density of surface wind speed and significant wave height for (*a*) June–September and (*b*) December–March. Lightest gray shade indicates that no altimeter ground track intersected the 2° by 2° box, medium gray represents 6 intersections, and black represents greater than 12 intersections.

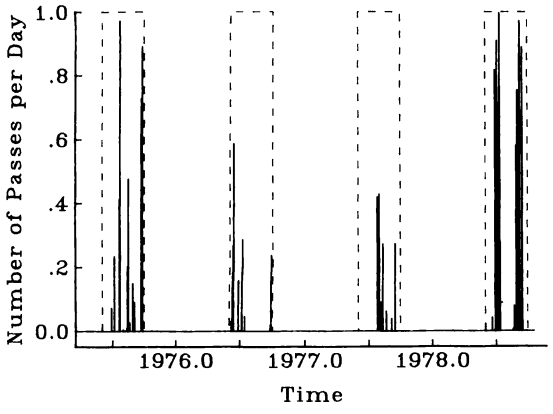

Fig. 2. Temporal distribution of GEOS 3 altimeter passes in the vicinity of 10°N, 200°E for the months June–September. The optimal time sampling is shown by the dashed line. A value of >0.5 indicates that the pass is less than 300 km from the point 10°N, 200°E.

later Seasat altimeter which carried a tape recorder. The GEOS 3 data density is highest near tracking stations and lowest in more remote areas of the world. Despite this relatively poor data distribution, averaging the GEOS 3 data over both space and time reveals significant seasonal variation in wind speed and sea state. Many of these seasonal features have not been reported previously. Moreover, the maps derived (Figures 3 through 6) from the GEOS 3 data show substantial hemispherical asymmetry in the seasonal variations in these quantities. Most of the seasonal variation occurs in the northern hemisphere, while winds and waves in the southern hemisphere are fairly steady.

Data Analysis

Return pulses of GEOS 3 altimeter data were processed by NASA Wallops Flight Center to extract wind speeds and wave heights [*Stanley and Dwyer*, 1980]. Surface wind speeds were computed using an algorithm developed by *Brown* [1979]. Comparisons of these wind speed estimates with ship and buoy measurements show good agreement (i.e., typical standard deviations of 3 m s^{-1}). The significant wave height algorithm used to process the GEOS 3 data is described in the work of *Fedor et al.* [1979]. Good agreement was also found between $H_{1/3}$ estimates from GEOS 3 data and ship and buoy measurements. For low sea conditions ($H_{1/3} < 4$ m) the accuracy of the GEOS 3 determined $H_{1/3}$ estimates is better than 0.75 m, and for medium sea conditions ($4 < H_{1/3} < 8$ m) estimated accuracies are 0.5 m.

In our analysis, only the short-pulse (intensive) mode data were used. Data points acquired over land or ice were edited. Spurious wind speed values of less than 0.01 m s^{-1} or greater than 45 m s^{-1} were also edited. Similarly, we edited sea states with values of less than 0.01 m or greater than 20 m. After editing, approximately 2.2 million of each data type were used to construct the maps.

As stated above, the distribution of GEOS 3 data is nonuniform. Coverage is sparse in many areas of the southern oceans. To examine the seasonal variations in wind speed and sea state, one would normally average all of the 3.5 years of GEOS 3 data into four different seasonal periods (i.e., winter, spring, summer, and fall). However, since we were also interested in displaying the spatial distribution of these quantities, it was necessary to use only two extended seasons. We chose the northern hemisphere summer season as June 1 through September 30 and the northern hemisphere winter season as December 1 through March 31. Some spatial resolution was gained by extending the time averages from 3 to 4 months.

After dividing the data into these two extended seasons, they were averaged into 2° by 2° areas. Figure 1*a* shows the data distributed for both wind speed and sea state (i.e.,they are nearly identical). The lightest gray shade indicates that no passes of GEOS 3 data intersected the 2° box. The intermediate gray tone indicates that 6 passes of data intersected the box while black boxes were intersected by more than 12 passes. From Figure 1*a* it is evident that summer wind speeds and sea states are poorly sampled over the southern Indian Ocean, the southeast Atlantic Ocean, and the east central Pacific Ocean. On the other hand, the North Pacific and most of the Atlantic are well sampled (i.e., 12–45 passes). The data distribution for the winter months (Figure 1*b*) is generally better. However, there is one large gap in the data in the South Atlantic. We have omitted this region and other large regions containing no data from further analysis.

The smaller data gaps remaining in the two data distributions (Figures 1*a* and 1*b*) are filled by using an interpolating filter. Consider the Gaussian filter

$$\rho(r) = \exp\left(\frac{-r^2}{2\sigma^2}\right) \tag{1}$$

where σ is the half width of the filter and

$$r = a(\theta^2 + \phi^2 \cos^2 \theta)^{1/2} \tag{2}$$

In (2), θ is latitude, ϕ is longitude, and a is the radius of the earth.

Wind speeds and sea states were smoothed and interpolated by convolving the filter (1) with the data multiplied by the data density. For continuous data this is

$$\bar{f}(\theta, \phi) = \frac{\int_0^{2\pi}\int_{-\pi/2}^{\pi/2} f(\theta_0, \phi_0) n(\theta_0, \phi_0) \rho(\theta - \theta_0, \phi - \phi_0) \cos\theta_0 \, d\theta_0 \, d\phi_0}{\int_0^{2\pi}\int_{-\pi/2}^{\pi/2} n(\theta_0, \phi_0) \rho(\theta - \theta_0, \phi - \phi_0) \cos\theta_0 \, d\theta_0 \, d\phi_0} \tag{3}$$

where $n(\theta, \phi)$ is the data density (number of passes per unit area), f is the function before smoothing and interpolation, and $\bar{f}$ is the smoothed and interpolated function.

In practice, (3) was approximated using the trapezoidal rule and integration steps of 2°. The half-width 2σ was chosen to be 600 km. This width was found to be a good compromise between the well-sampled and the poorly sampled regions. A variable width filter based upon the data distribution was not used because the resulting maps are difficult to interpret.

This smoothing operation not only low-pass filters the data in the space domain, but it also improves the time distribution. As shown in the data distribution maps, each 2° by 2° area is intersected by an average of only six passes. (We consider an intersection as one data point, although it is the average of about 30 observations.) Significant aliasing of short-period meteorological variations into seasonal variations could develop with so few samples distributed over the 3.5-year period. The smoothing operation, described by (3), improves the time sampling because it incorporates data from a larger area (about 600 km in diameter). To illustrate how the time sampling is improved by spatial averaging, we investi-

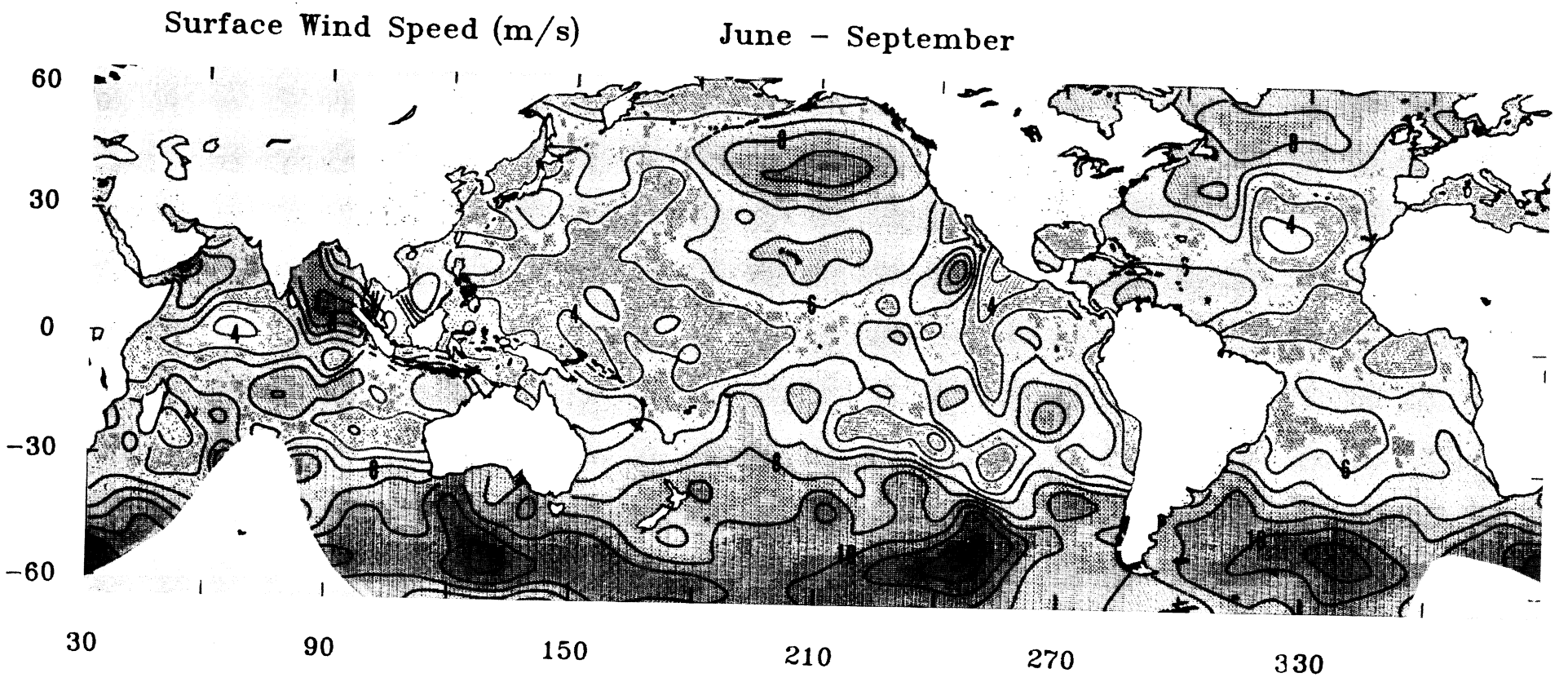

Fig. 3*a*

Fig. 3. Contour maps of surface wind speed in meters per second, (*a*) June–September and (*b*) December–March. In both hemispheres the highest average wind speeds occur at mid-latitudes (35° to 65°) during their winter months. Wind speeds in tropical regions (±30°) are relatively low.

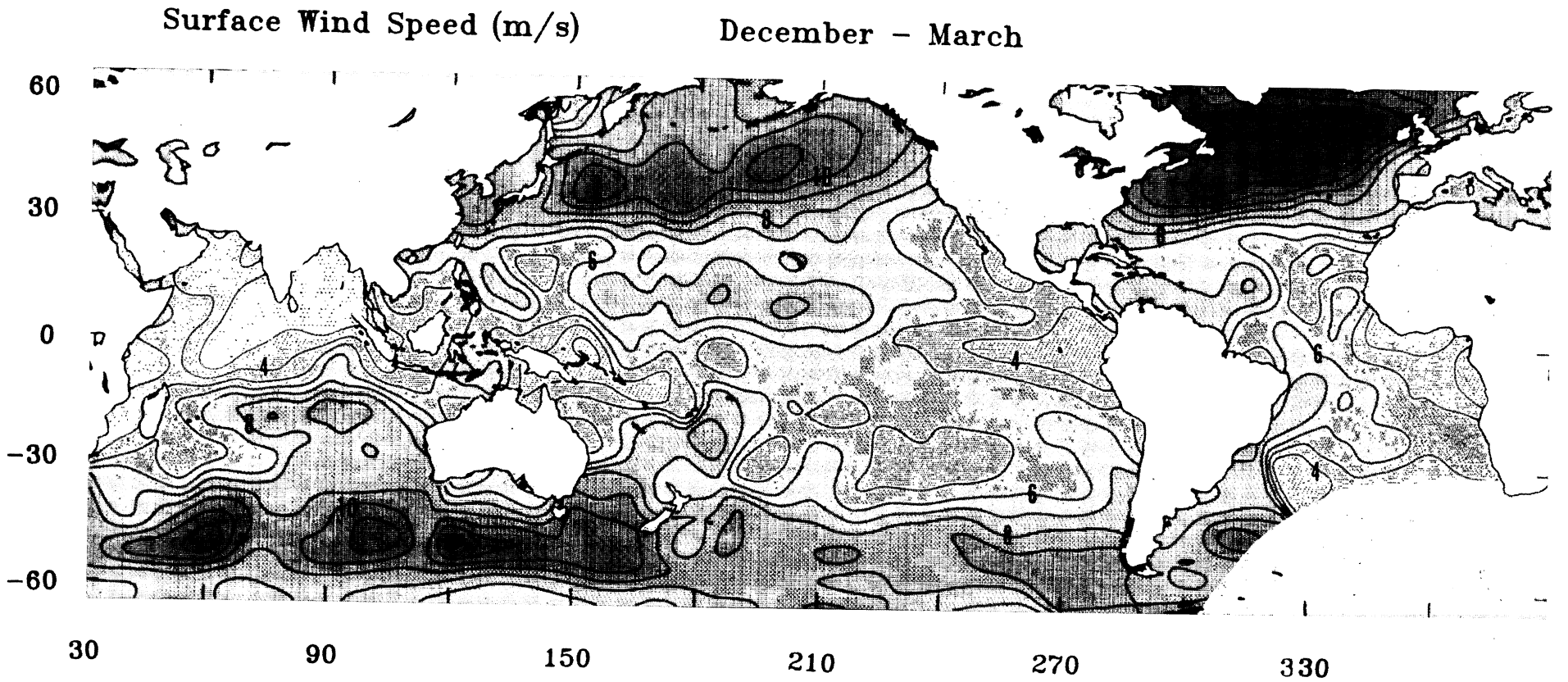
Surface Wind Speed (m/s)
December - March
60
30
0
-30
-60
30
90
150
210
270
330

Fig. 3*b*

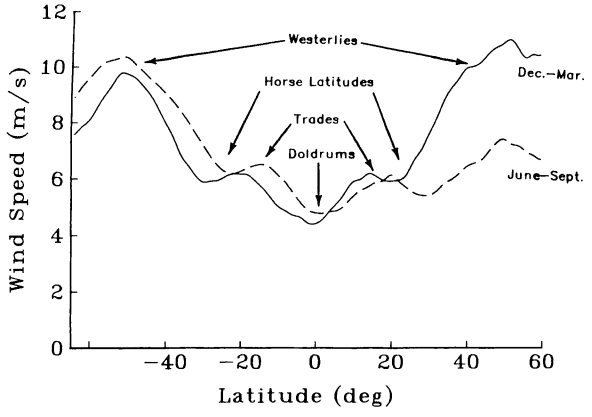

Fig. 4. Wind speed averaged over longitude for two seasonal periods, June–September (dashed curve) and December–March (solid curve). Arrows point to the major zonal wind patterns.

gated the June–September time distribution (Figure 1*a*) for an area in the central Pacific centered at 10°N, 200°E. For each day of the mission, we convolved the ground tracks with the Gaussian window (equation (1)) centered at the point. The results are shown in Figure 2, where the number of passes per day is plotted versus time. An altimeter ground track which intersected the point 10°N, 200°E was assigned a density of one pass per day. Passes lying within 300 km of the point have densities greater than 0.5, while more distant passes have lower densities. Also shown in Figure 2 is the optimal time window (dashed line) corresponding to one intersection for every day during the months June–September. The actual time sampling is far from optimal, although there are 31 days where the number of passes per day exceeds 0.1. Because of this incomplete time sampling the actual seasonal averages and those presented below may differ substantially.

Results and Discussion

Contour maps of wind speed for boreal summer and winter are shown in Figures 3*a* and 3*b*, respectively. The contour interval is 1 m s^{-1}. Areas between contours are shaded in various gray tones to highlight the map features. When interpreting these maps, one must also examine the data distribution (Figures 1*a* and 1*b*). For example, the June–September data density is low in the southeast Pacific. This poor sampling results in a curious pattern of wind speed highs and lows. Three areas, two on the June–September map and one on the December–March map, did not have sufficient data density to be contoured. These areas are left blank on the contour maps.

During the austral winter (June–September) the largest wind speeds of 8 to 12 m s^{-1} occur in the southern hemisphere between latitudes of −40° and −60°. This band of high wind speed, which also appears on the Seasat-derived maps [*Chelton et al.*, 1981; *Mognard et al.*, 1983], surrounds the Antarctic continent and is associated with mid-latitude winter storms. Highest average wind speeds (> 10 m s^{-1}) generally occur away from continents and are centered over the Antarctic Circumpolar Current. Other more localized areas of high wind speed appear in the North Atlantic, the Gulf of Alaska, south of the Baja California Peninsula, and in the Bay of Bengal. The latter feature is associated with monsoons. The high wind speed area near Baja California is produced by tropical cyclones such as hurricane Iva (August 1978). This hurricane was also sampled by the Seasat altimeter [*Gonzalez et al.*, 1982]. As noted by *Chelton et al.* [1981], both the North Atlantic and the North Pacific are characterized by light winds during boreal summer.

The patterns of wind speed change drastically between summer and winter (Figure 3). As expected, wind speeds are very high in the North Atlantic and North Pacific during its winter. Indeed, the highest average wind speeds (> 14 m s^{-1}) in the world's oceans occur in the northern North Atlantic during this period. It is interesting that there is not a complementary decrease in southern hemisphere wind speeds between the austral winter and summer.

Another interesting feature that appears most strongly in the December–March wind speed map is the correlation between high wind speed and strong ocean currents. Local wind speed maxima occur over the Antarctic Circumpolar Current, the Kuroshio, and the Gulf Stream. It is well known that basin-wide gyres associated with these currents are maintained by the prevailing winds [*Munk*, 1950]. The more localized wind speed maxima over the western boundary currents, however, may be produced by large sea surface temperature contrasts.

For centuries, sailors have known of the zonal wind patterns such as the westerlies, the horse latitudes, the trades, and the doldrums. These patterns appear on the GEOS 3 derived wind speed maps (Figures 3*a* and 3*b*), although spurious contours over areas of low data density mask the patterns between +30° and −30°. To enhance these zonal wind speed patterns and their seasonal variation, we averaged all of the 2° boxes into latitudinal zones. The data in each box were weighted by the number of passes through the box. The results are shown in Figure 4, where average wind speed for each seasonal period is plotted as a function of latitude. The zonal wind patterns are evident as local maxima and minima in this figure. The 5° to 10° shift in the zonal patterns between the two seasonal periods is also apparent. The most striking feature of the zonal wind speed patterns is the large asymmetry in the summer-to-winter wind speed variation between the two hemispheres. In particular, the westerlies in the northern hemisphere increase by approximately 50% between summer and winter, whereas the corresponding increase in the southern hemisphere is only 10%. This is in agreement with global atmospheric angular momentum variations which show a large seasonal angular momentum variation in the northern hemisphere and a smaller variation in the southern hemisphere [*Hide et al.*, 1980; *Rosen and Salstein*, 1981].

Qualitatively, these geographical and seasonal variations in wind speed have been known for centuries. Modern compilations of global wind speeds from ship reports are more quantitative, but they are often expressed as crude probability estimates [*U.S. Naval Oceanographic Office*, 1963] owing to the large errors involved and poor global sampling. The GEOS 3 results shown here demonstrate that reliable estimates of wind speed can be obtained globally from future satellite altimeters. Moreover, observations by satellite are uniform in quality, and unlike ships which try to avoid storms, the distribution of satellite observations is unbiased.

The global distribution of significant wave height and its seasonal variation is perhaps less well known, especially in the southern ocean. Since waves are generated by winds, one would expect a high correlation between wind speed and $H_{1/3}$. Significant wave height maps for the periods June–September

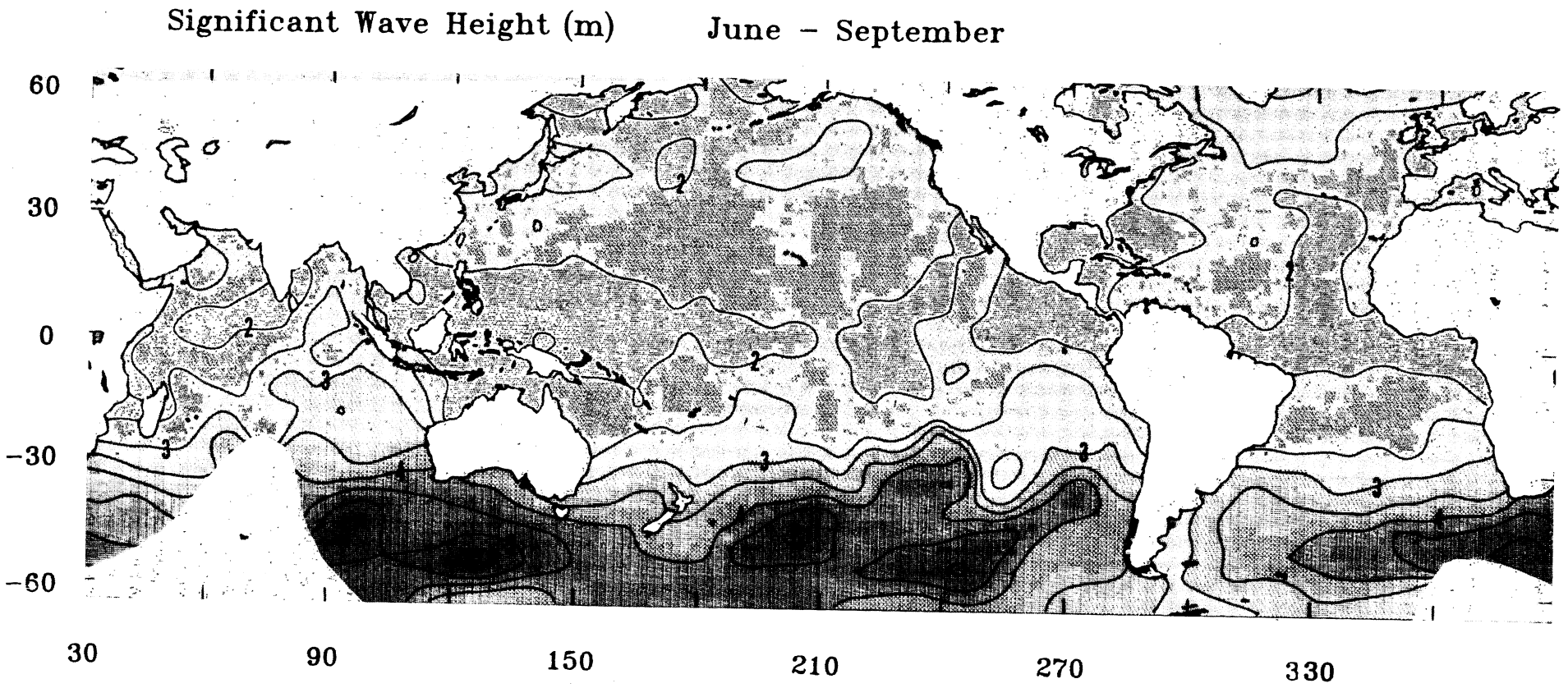
Significant Wave Height (m)
June – September
60
30
0
-30
-60
30
90
150
210
270
330

Fig. 5*a*

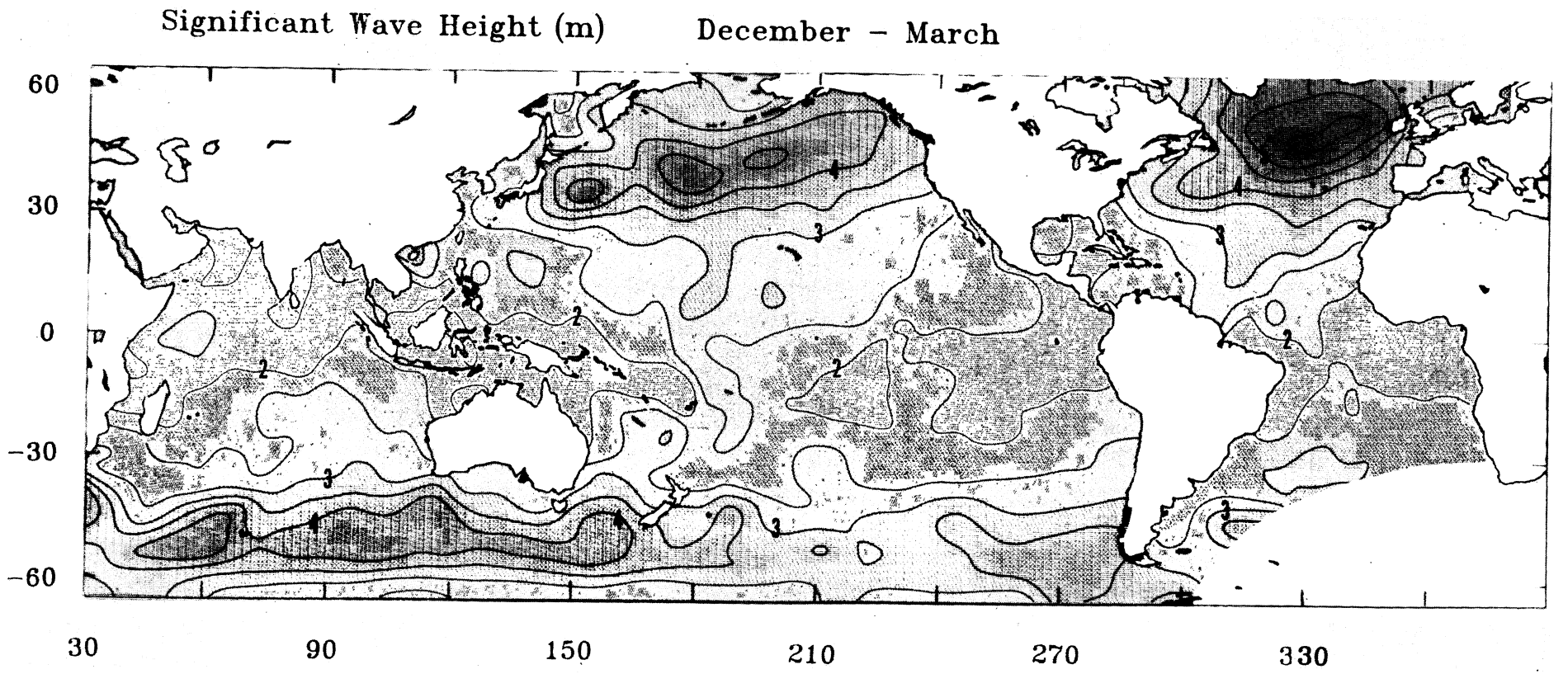

Fig. 5*b*

Fig. 5. Contour maps of significant wave height in meters (i.e., the height of the highest 1/3 waves), (*a*) June–September and (*b*) December–March. Contour interval is 0.5 m.

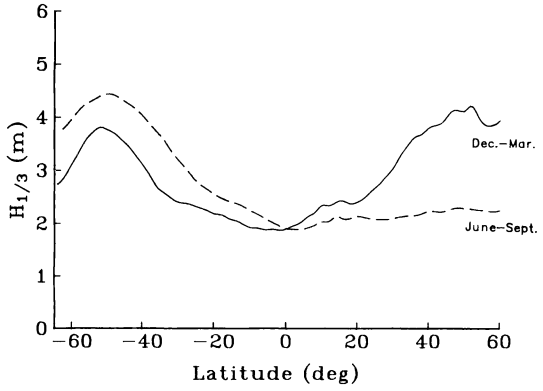

Fig. 6. Significant wave height averaged over longitude for the two seasonal periods, June–September (dashed line) and December–March (solid line). Zonal wave patterns reflect only the major features of the zonal wind patterns.

and December–March are shown in Figures 5*a* and 5*b*, respectively. Again when interpreting these maps one must also examine the data distribution maps.

As expected, features in the significant wave height maps (Figures 5*a* and 5*b*) generally reflect features in the wind speed maps (Figures 3*a* and 3*b*). For example, during boreal summer, average wave heights are low (2 to 3 m) in both the North Atlantic and the North Pacific. In the southern oceans, significant wave heights are highest (4 to 5.5 m) during this period. Wave heights are generally low in equatorial regions because of low wind speeds in these areas. Neither the monsoons in the Bay of Bengal nor the hurricanes near Baja, California, generate high waves even though these features appear as maxima in the wind speed maps. Since the wind speed and sea state data distributions are identical, we believe the lack of $H_{1/3}$ maxima is due to the small fetch of these localized wind patterns.

The significant wave height map for boreal winter shows a dramatic increase in $H_{1/3}$ in the northern ocean areas and only a small decrease in the southern oceans. This reflects the seasonal variation in wind speed. Like the average wind speed, the highest waves (> 5.5 m) occur in the North Atlantic during its winter. Localized wave height maxima occur over the Kuroshio and Gulf Stream as well.

The zonal wave patterns are illustrated in Figure 6, where longitudinally averaged significant wave height is plotted against latitude. The dominant zonal wave patterns are associated with the westerlies and therefore occur at mid-latitudes. Again note the dramatic seasonal change in the northern hemisphere while the seasonal variation in the southern hemisphere is relatively small. There is no pronounced local minimum corresponding to the horse latitudes, although a hint of a minimum appears at $+20°$ on the December–March profile. The trade winds do not produce a local maximum in the zonal wave heights. There is, however, a wave height minimum corresponding to the doldrums. Moreover, this minimum shifts by about 5° to 10° between the two seasonal periods, reflecting the shift in the zonal wind patterns.

The smoothness of the zonal wave patterns as compared with the zonal wind patterns is due to wave propagation. Waves generated by storms in the mid and high latitudes propagate to lower latitudes where they are detected by the altimeter [*Mognard*, 1982]. This propagation effect is most apparent on the December–March map where the central ocean areas, with their large aperture of exposure, have higher waves than coastal areas where waves can approach from only one side.

Summary

1. In addition to measuring the shape of the sea surface, the GEOS 3 altimeter measured wind speed and significant wave height over the world's oceans. Data density is higher near tracking stations and lower in more remote areas.

2. From nearly 4 years of data, we constructed global maps of the average wind speed during two extended seasons, June–September and December–March. Large seasonal variations in wind speed occur in the northern oceans, while in the southern oceans the wind does not vary much between seasons. Longitudinal averaging of these maps reveals the well-known zonal wind patterns such as the westerlies, the horse latitudes, the trades, and the doldrums.

3. Global significant wave height maps for the two seasonal periods reflect most of the features on the wind speed maps. Average wave heights are greater than 5.5 m in the North Atlantic during the period December–March and diminish to less than 2.5 m during June–September. A similar large seasonal variation in wave height was not observed in the southern oceans. This hemispherical asymmetry in the seasonal variation of $H_{1/3}$ is more apparent in the longitudinally averaged $H_{1/3}$. Zonal patterns of $H_{1/3}$ reflect the zonal wind patterns, although the relative maxima and minima are less distinct because of wave propagation.

Acknowledgments. We thank Bob Cheney and Bruce Douglas for their comments and help in preparing this report.

References

Brown, G. S., Estimation of surface wind speeds using satellite-borne radar measurements at normal incidence, *J. Geophys. Res.*, *84*, 3974–3978, 1979.

Charnock, H., Wind stress on a water surface, *Q. J R. Meteorol. Soc.*, *81*, 639–640, 1955.

Chelton, D. B., K. J. Hussey, and M. E. Parke, Global satellite measurements of water vapor, wind speed and wave height, *Nature*, *294*, 529–532, 1981.

Cox, C., and W. Munk, Statistics of the sea surface derived from sun glitter, *J. Mar. Res.*, *13*, 198–227, 1954.

Fedor, L. S., T. W. Godbey, J. F. R. Gower, R. Guptill, G. S. Hayne, C. L. Rufenach, and E. J. Walsh, Satellite altimeter measurements of sea state—An algorithm comparison, *J. Geophys. Res.*, *84*, 3991–4001, 1979.

Gonzalez, F. I., T. W. Thompson, W. E. Brown, Jr., and D. E. Weissman, Seasat wind and wave observations of northeast Pacific hurricane Iva, August 13, 1978, *J. Geophys. Res.*, *87*, 3431–3438, 1982.

Hide, R., N. T. Birch, L. V. Morrison, D. J. Shea, and A. A. White, Atmospheric angular momentum fluctuations and changes in the length of day, *Nature*, *286*, 114–117, 1980.

McPherson, R. D., K. H. Bergman, R. E. Kistler, G. E. Rasch, and D. S. Gordon, The NMC operational global data assimilation system, *Mon. Weather Rev.*, *107*, 1445–1461, 1979.

Mognard, N. M., Application of satellite radar altimetry to the determination of sea state, thesis, Univ. Paul Sabatier de Toulouse, Toulouse, France, 1982.

Mognard, N., and B. Lago, The computation of wind speed and wave heights from GEOS 3 data, *J. Geophys. Res.*, *84*, 3979–3986, 1979.

Mognard, N. M., W. J. Campbell, R. E. Cheney, and J. G. Marsh, Southern ocean mean monthly waves and surface winds for winter 1978 by Seasat radar altimeter, *J. Geophys. Res.*, *88*, 1736–1744, 1983.

Munk, W. H., On the wind-driven ocean circulation, *J. Meterol.*, *7*, 79–93, 1950.

Parsons, C. L., GEOS 3 wave height measurements: An assessment during high sea state conditions in the North Atlantic, *J. Geophys. Res.*, *84*, 4001–4020, 1979.

Rosen, R. D., and D. A. Salstein, Variation in atmospheric angular momentum, 1 January 1976–31 December 1980, *Tech. Rep. A345-T1*, Environ. Res. & Technol., Inc., Concord, Mass., 1981.

Stanley, H. R., The GEOS 3 project, *J. Geophys. Res.*, *84*, 3779–3783, 1979.

Stanley, H. R., and R. E. Dwyer, *NASA Wallops Flight Center GEOS 3 Altimeter Data Processing Report*, 128 pp., National Aeronautics and Space Administration, Washington, D. C., 1980.

Sverdrup, H. U., Wind-driven currents in a baroclinic ocean; with application to the equatorial currents of the eastern Pacific, *Proc. Natl. Acad. Sci. U.S.A.*, *33*, 318–326, 1947.

U.S. Naval Oceanographic Office, *Oceanographic Atlas of the North Atlantic Ocean, Publ. 700*, Bay St. Lewis, Miss., 1963.

Walsh, E. J., Extraction of ocean wave height and dominant wavelength from GEOS 3 altimeter data, *J. Geophys. Res.*, *84*, 4003–4010, 1979.

Wu, J., Wind-stress coefficients over sea surface near neutral conditions—A revisit, *J. Phys. Oceanogr.*, *10*, 727–740, 1980.

R. W. Agreen and D. T. Sandwell, Geodetic Research and Development Laboratory, National Geodetic Survey, National Oceanic and Atmospheric Administration, Charting and Geodetic Services, Rockville, MD 20852.

(Received May 5, 1983;
revised August 25, 1983;
accepted October 25, 1983.)